ChemComm

COMMUNICATION

View Article Online
View Journal | View Issue

Cite this: *Chem. Commun.*, 2024, **60**, 11588

Received 30th July 2024,
Accepted 18th September 2024

DOI: 10.1039/d4cc03818e

rsc.li/chemcomm

An ultralow iridium-incorporated Ni–Fe bimetallic–organic framework for efficient oxygen evolution reaction†

Zixiong Wang, Zhaoxin Zhou, Qi Zhang, He Zhu* and Shiping Zhu*

The development of electrocatalysts is of vital importance to the OER. In this work, an optimized MOF electrode, Ir-NiFe-btz/NF, was synthesized by incorporating ultralow levels of Ir nanoparticles into an ionic bimetallic MOF. Under alkaline conditions, the prepared MOF electrode demonstrated outstanding OER activity and stability with a low overpotential of 182 mV to reach 10 mA cm^{-2} and no obvious increase of overpotential in a chronovoltammetry test over 100 hours at 100 mA cm^{-2}.

Considering the global energy crisis and numerous environmental challenges caused by the depletion and combustion of fossil fuels, it is essential to develop clean, sustainable, and renewable energy alternatives.[1,2] Hydrogen, as a novel green energy source, distinguishes itself through its renewability, zero pollution after combustion, and wide distribution of sources.[3–5] Among various methods for hydrogen production, considerable emphasis has been laid on electrochemical water splitting because of its safety, high efficiency, and capability for large-scale industrial production.[6,7] However, the anodic half-reaction of water splitting, *i.e.* the oxygen evolution reaction (OER), is kinetically sluggish, involving a four-electron-transfer process that demands high overpotential to drive.[8] Developing cutting-edge OER electrocatalysts has therefore been prioritized to break the technological bottleneck and fulfill the need for industrial hydrogen production.

Recent decades have witnessed rapid development and deep research in metal–organic frameworks (MOFs).[9,10] As an emerging class of porous materials assembled by metal ions and organic ligands, MOFs have been identified as prospective OER catalysts because of their abundant active sites, designable structures, and varied components.[11,12] Compared to monometallic MOFs, bimetallic MOFs, especially NiFe-based ones, possess better OER activity due to the facilitated charge transport, optimized electronic structure, and strong synergistic effect between metal centers.[13] For example, Dong *et al.* found the strongest synergistic effect in NiFe-MOF when regulating the Ni/Fe ratio at 1 : 1, significantly enhancing adsorption between active sites and species, leading to superior OER activity.[14] Wang and co-workers fabricated a self-supported Fe-doped Ni-HHTP nanowire array with excellent OER performance because Fe sites enabled additional hydrogen bond formation between intermediates and adjacent layers.[15] Zhu *et al.* reported the fabrication of ultrathin iron-rich NiFe-MOF nanosheets, and their great OER activity was attributed to the combination of the unique nanostructure and the strong coupling effect between Ni and Fe active sites.[16] Although these results demonstrate the great potential of NiFe-MOFs as OER electrocatalysts, their wide application is still hampered by their low intrinsic conductivity and unsatisfactory electrochemical stability.

In this study, a NiFe-bimetallic ionic MOF-based electrode with excellent OER electrochemical activity was designed based on two aspects. First, the use of ionic MOFs: the presence of counter ions within the charged framework can not only enhance the overall intrinsic conductivity of MOFs through facilitating charge transport within them but also allows for exchange with the OH^- in the electrolyte and promotes contact between the OH^- and active sites.[17,18] Second, the incorporation of iridium (Ir) in MOFs: incorporating small amounts of noble metals can modulate the chemical and electronic structure of the catalyst, which effectively enhances the inherent activity.[19] Additionally, the presence of Ir can improve the corrosion resistance and stability of the electrocatalysts in alkaline electrolytes, especially at large current densities. Specifically, NiFe-btz (btz: 1,4-bis(4*H*-1,2,4-triazol-4-yl)benzene), a cationic MOF with Cl^- as the counterion, was *in situ* grown on nickel foam (NF). The obtained NiFe-btz/NF was then incorporated with ultralow amounts of Ir nanoparticles to prepare the final electrode (Ir-NiFe-btz/NF), which demonstrated outstanding catalytic properties proved by the low overpotential of 182 mV at 10 mA cm^{-2} and the small Tafel slope of 38 mV dec^{-1}.

School of Science and Engineering, The Chinese University of Hong Kong, Shenzhen, 518172, Guangdong, P. R. China.
E-mail: zhuhe@cuhk.edu.cn, shipingzhu@cuhk.edu.cn

† Electronic supplementary information (ESI) available. See DOI: https://doi.org/10.1039/d4cc03818e

Its excellent stability was demonstrated by the negligible increase of overpotential for 100 hours at the large current density of 100 mA cm^{-2}. Meanwhile, the synergistic effect brought by the bimetallic system and the reconstructed products after the OER test was thoroughly studied. This work provides future scope and strategies for developing novel ionic MOF-based electrocatalysts for the OER.

The Ir-NiFe-btz/NF electrode was fabricated *via* a two-step solvothermal reaction. As illustrated schematically in Fig. S1 (ESI†), bimetallic NiFe-btz was *in situ* prepared on NF in a water/DMSO solution at 120 °C initially, with NF serving as the substrate and the Ni source, Fe^{3+} as the etching agent and the Fe source, and btz as the ligand. Next, the prepared NiFe-btz/NF was immersed into an aqueous solution of $IrCl_3 \cdot xH_2O$, which was maintained at 80 °C for 12 hours to incorporate Ir nanoparticles, yielding the final Ir-NiFe-btz/NF electrode. In addition, monometallic MOF electrodes, Ni-btz/NF and Fe-btz/NF, with their corresponding Ir-incorporated electrodes, Ir-Ni-btz/NF and Ir-Fe-btz/NF, were also prepared by the same procedure for comparison.

The morphology of the as-prepared MOF electrodes was studied using scanning electron microscopy (SEM) and transmission electron microscopy (TEM). SEM images revealed the distinctive 3D macroporous structure and the smooth surface of NF after being treated with 1 M HCl solution (Fig. S2, ESI†). As shown in Fig. S3 (ESI†), a homogenously distributed bulk structure of NiFe-btz was observed on the surface of NF after the first solvothermal reaction. Compared with the monometallic MOF/NF electrodes (Fig. S4, ESI†), the bimetallic NiFe-btz was more densely packed on the substrate, benefitting from the continuously released Ni^{2+} from the Fe^{3+} etching, which effectively confined the nucleation sites close to the NF substrate. The Brunauer–Emmett–Teller (BET) specific surface area of NiFe-btz was measured to be ~133 m^2 g^{-1}, and its pore size distribution indicated the existence of mesopores, which was favorable for Ir incorporation and electrochemical reaction kinetics (Fig. S5, ESI†).

After Ir incorporation, the morphology of Ir-NiFe-btz shown in Fig. 1a and b perfectly inherited the pristine MOFs without any obvious differences. The TEM image displayed a multilayered stacked bulk structure of NiFe-btz (Fig. S6, ESI†), consistent with the SEM results, and the lattice spacings of 1.342 nm and 0.813 nm in the high-resolution TEM (HRTEM) image (Fig. S7, ESI†) were assigned to the (101) and (002) crystal planes of NiFe-btz, respectively. As seen in Fig. 1c, the incorporated Ir nanoparticles were firmly anchored and well-dispersed in the NiFe-btz with an average particle size of ~2 nm. The generation of Ir nanoparticles was verified by a distinct interplanar spacing of 0.225 nm (Fig. 1d), which corresponded to the (111) crystal plane of Ir. Furthermore, the high-angle annular dark-field scanning TEM (HAADF-STEM) image and energy dispersive X-ray (EDX) elemental mapping images showed the uniformly distributed Ir, Ni, Fe, Cl, and N elements in the selected area (Fig. S8, ESI†), demonstrating the presence of Ni and incorporated Ir in Ir-NiFe-btz. Inductively coupled plasma optical emission spectrometry (ICP-OES) was applied to study the quantity of Ni, Fe, and Ir in the Ir-NiFe-btz, and the result

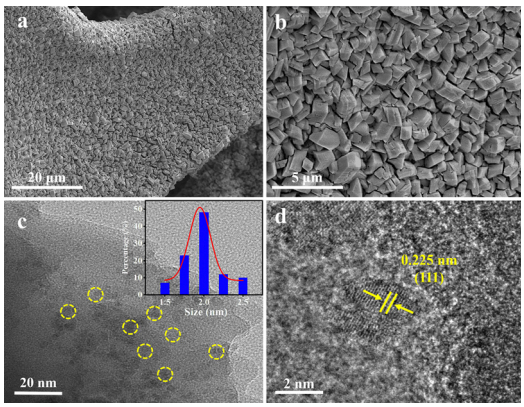

Fig. 1 SEM images of (a) and (b) Ir-NiFe-btz *in situ* grown on an NF substrate. TEM images of (c) Ir-NiFe-btz (Ir nanoparticles were labelled in yellow circles), and (d) lattice spacing of Ir incorporated in Ir-NiFe-btz.

indicated the Ni/Fe/Ir atomic ratio of 3.8 : 1 : 0.005, proving the existence of an ultralow level of Ir in the prepared electrode.

The crystal structures of the prepared MOF electrodes were examined by powder X-ray diffraction (PXRD). As seen in Fig. S9 (ESI†), each PXRD pattern of the prepared mono/bimetallic MOF electrodes matched with the simulated Ni-btz (CCDC no. 1969913),[20] indicating that they were all successfully synthesized in a similar structure. After Ir incorporation, the diffraction peaks of Ir-NiFe-btz shifted a little to the lower angle region, implying that the Ir incorporation caused an expansion of the interplanar distance but did not change the original MOF structure. X-ray photoelectron spectroscopy (XPS) was then applied to analyze the compositions and chemical states of NiFe-btz and Ir-NiFe-btz. The presence of C, N, O, Cl, Ni, and Fe in NiFe-btz, as well as C, N, O, Cl, Ni, Fe, and Ir in Ir-NiFe-btz, was well demonstrated by the XPS survey spectrum (Fig. S10, ESI†). In the high-resolution Ni 2p spectrum (Fig. 2a), two prominent peaks at 855.88 eV (Ni $2p_{3/2}$) and 873.72 eV (Ni $2p_{1/2}$) were assigned to the Ni^{2+} from Ir-NiFe-btz, proving the existence of Ni^{2+} in MOFs generated from Fe^{3+} etching. In addition, the Ni^{2+} peaks in Ir-NiFe-btz observed a positive shift of 0.36 eV compared with those from the NiFe-btz. In Ir-NiFe-btz, charge transferred from Ir to Ni because of the difference in electronegativity, and the total negative charge slightly increased. This resulted in a stronger attraction between the Ni 2p electrons and the nucleus, thus raising the binding energy of the Ni 2p orbital. The electronic structure modification

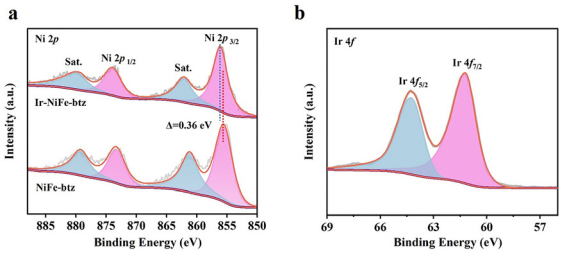

Fig. 2 High-resolution XPS spectra of (a) Ni 2p and (b) Ir 4f in NiFe-btz and Ir-NiFe-btz electrodes.

of the MOFs proved the strong interaction between Ir nanoparticles and pristine NiFe-btz, which was expected to enhance the electrocatalytic performance of Ir-NiFe-btz. Fig. S11 (ESI†) displays two peaks at 709.1 eV and 723.7 eV assigned to Fe^{2+}. No other peaks were seen in the spectra, indicating that all Fe elements in the prepared MOF electrodes were presented in the form of Fe^{2+}, and were reduced from Fe^{3+} after oxidizing Ni. The high-resolution Ir 4f area (Fig. 2b) could be deconvoluted into two peaks at 61.23 eV and 64.43 eV, corresponding to the Ir $4f_{7/2}$ and Ir $4f_{5/2}$ of Ir nanoparticles. XPS analysis, together with all previous characterization results, proved the successful formation of Ir-NiFe-btz.

The OER performances of the as-synthesized NiFe-btz/NF and Ir-NiFe-btz/NF electrodes, together with Ni-btz/NF, Fe-btz/NF, Ir-Ni-btz/NF, Ir-Fe-btz/NF, benchmark RuO_2 and bare NF, were next evaluated in 1 M KOH solution. Linear sweep voltammetry (LSV) curves (Fig. 3a and Fig. S12, ESI†) were recorded at a scan rate of 5 mV s^{-1} and those obtained from the reverse sweep (Fig. S13, ESI†) were employed to identify the overpotential at 10 mA cm^{-2} to rule out the influence of the anodic peak positioned at 1.36 V (*versus* RHE) that resulted from the metal oxidation prior to water oxidation. These curves demonstrated the superior catalytic activity of Ir-NiFe-btz/NF, needing the smallest overpotential of 182 mV to reach the current density of 10 mA cm^{-2}, which significantly exceeded the values of NiFe-btz/NF (225 mV), Fe-btz/NF (257 mV), Ni-btz/NF (298 mV), Ir-Ni-btz/NF (221 mV), Ir-Fe-btz/NF (203 mV), RuO_2 (400 mV) and bare NF (370 mV) at the same current density (Fig. S14, ESI†). Furthermore, to achieve a larger current density of 100 mA cm^{-2}, Ir-NiFe-btz/NF required an overpotential as low as 232 mV, being 71 mV lower than that of NiFe-btz/NF and outperforming those of Fe-btz/NF (320 mV), Ni-btz/NF (440 mV), Ir-Ni-btz/NF (285 mV), Ir-Fe-btz/NF (260 mV) and bare NF (510 mV), indicating the considerable contribution of Ir incorporation toward the enhanced OER activity (Fig. S15, ESI†). The inherent kinetics of MOF electrodes were examined by analyzing Tafel plots originating from the corresponding polarization curves. As shown in Fig. 3b and Fig. S16 (ESI†), Ir-NiFe-btz/NF had the smallest Tafel slope of 38 mV dec^{-1} compared to NiFe-btz/NF (56 mV dec^{-1}) and was comparatively lower than those of Fe-btz/NF (68 mV dec^{-1}), Ni-btz/NF (85 mV dec^{-1}), Ir-Ni-btz/NF (69 mV dec^{-1}), Ir-Fe-btz/NF (52 mV dec^{-1}), RuO_2 (193 mV dec^{-1}) and bare NF (104 mV dec^{-1}), proving its more rapid charge transfer and improved OER kinetics. Combining the overpotential at 10 mA cm^{-2} and Tafel slope for comparison, Ir-NiFe-btz/NF surpassed many previously reported Ir-based and NiFe-MOF-based OER catalysts (Fig. 3c and Table S1, ESI†).

To further evaluate the electrochemical kinetics and conduct a deeper analysis of the improved OER performance, electrochemical impedance spectroscopy (EIS) was applied on MOF electrodes in the frequency range of 0.1–10^5 Hz. Based on the Nyquist plots measured at 1.55 V (*versus* RHE), Ir-NiFe-btz/NF revealed the lowest R_{ct} value of 1.2 Ω, which distinguished itself from NiFe-btz/NF (1.8 Ω), Fe-btz/NF (2 Ω), Ni-btz/NF (7.7 Ω), Ir-Ni-btz/NF (1.8 Ω), Ir-Fe-btz/NF (1.4 Ω), RuO_2 (8.7 Ω) and bare NF (11.9 Ω) (Fig. 3d and Fig. S17, ESI†). The reduced R_{ct} value suggested a more efficient electron transport and the OER process was therefore expected to be comparatively smooth. Besides, cyclic voltammetry (CV) scanning at varying rates was used to study the electrochemical surface areas (ECSA) derived from the double-layer capacitance (C_{dl}) (Fig. S18–S21, ESI†). As depicted in Fig. 3e, Ir-NiFe-btz/NF exhibited the largest active surface area with a C_{dl} value of 12.6 mF cm^{-2}, almost twice that of NiFe-btz/NF (6.5 mF cm^{-2}) and was nearly four times that of bare NF (3.2 mF cm^{-2}). This suggested that the incorporated Ir nanoparticles could serve as active species that enhanced the intrinsic OER activity of the MOF electrode, which corresponded to the smallest R_{ct} value above as well. Besides, through the comparison of the performances between the monometallic and bimetallic MOF electrodes, incorporated with Ir or not, it could be concluded that the synergistic effect brought by Ni and Fe in the MOF was also crucial for boosting the OER activity, as indicated by the overall better performance of the bimetallic MOF electrodes over monometallic ones (Fig. S22–S24, ESI†).

The catalytic stability of NiFe-btz/NF and Ir-NiFe-btz/NF was thereafter examined by chronovoltammetry test at 100 mA cm^{-2} for 100 hours (Fig. 3f). Throughout the whole process, the overpotential of NiFe-btz/NF increased by 78 mV. As for Ir-NiFe-btz/NF, its overpotential remained at 450 mV with a negligible fluctuation of 5 mV up and down. In addition, Ir-NiFe-btz/NF after the stability test still had a polarization pattern similar to the one before the test without practical current density reduction (Fig. S25, ESI†). These results suggested the remarkable sustainability of the Ir-NiFe-btz electrode brought from the Ir incorporation.

The Ir-NiFe-btz after the OER test (post-Ir-NiFe-btz) was characterized by PXRD, XPS, SEM, and TEM to unveil its detailed structural and compositional information. As shown in Fig. S26 (ESI†), the PXRD pattern indicated a reduced crystallinity of post-Ir-NiFe-btz, with only two peaks located at 11.0° and 26.0° that could be assigned to the pristine MOF. At the same time, the two new peaks at 20.0° and 25.0° represented the generation of NiOOH, and the new peak at 22.0°

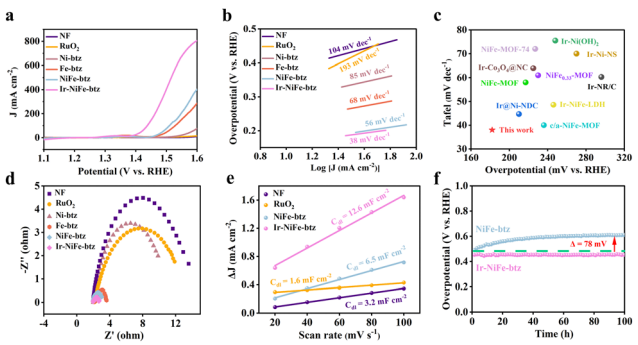

Fig. 3 Electrocatalytic performance of the prepared electrodes. (a) LSV curves. (b) Tafel plots. (c) OER activity comparison of Ir-NiFe-btz/NF with recently reported bimetallic NiFe-MOF-based and Ir-based electrocatalysts. (d) Nyquist plot. (e) Double-layer capacitance (C_{dl}). (f) Chronovoltammetry curve of NiFe-btz/NF and Ir-NiFe-btz/NF at 100 mA cm^{-2} for 100 hours.

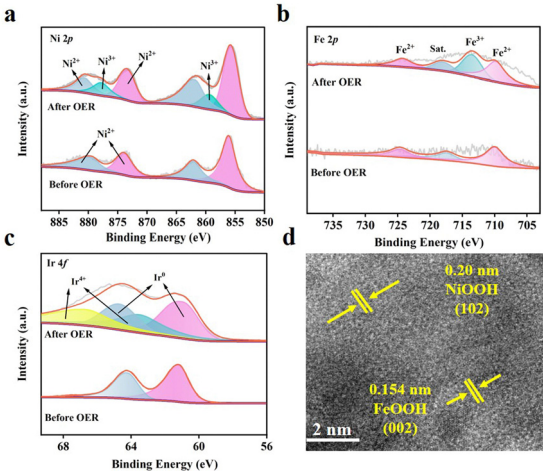

Fig. 4 High-resolution XPS spectra of (a) Ni 2p, (b) Fe 2p, and (c) Ir 4f of Ir-NiFe-btz before and after the OER. (d) HRTEM image of post-Ir-NiFe-btz.

corresponded to the generation of FeOOH.[21] The XPS survey spectrum (Fig. S27, ESI†) of post-Ir-NiFe-btz revealed the presence of Ir, Ni, Fe, C, N, Cl, and O, which was the same as the pristine MOFs. In the high-resolution Ni 2p spectra (Fig. 4a), two extra peaks denoting Ni^{3+} were seen, proving that NiOOH was generated during the OER test.[22] Similarly, a new peak, identified as Fe^{3+}, emerged in the high-resolution Fe 2p spectrum at 714.1 eV (Fig. 4b), signifying the iron oxidation and the possible formation of FeOOH during the OER. As for the Ir, a pair of new peaks at 63.6 and 66.8 eV was attributed to Ir^{4+} in its high-resolution 4f spectrum (Fig. 4c), proving that metallic Ir had been partially oxidized to IrO_2 upon the OER. After the water oxidation, the SEM image (Fig. S28, ESI†) showed that the original MOF morphology was partially maintained but with a rougher surface. This was because NiOOH and FeOOH were generated and covered on the surface during the OER process, resulting in a long-range disordered and short-range ordered structure. The HRTEM image further revealed the generation of metal oxyhydroxides after water oxidation, where clear lattice fringes of 0.20 nm represented the (102) lattice plane of NiOOH and 0.154 nm was aligned to the FeOOH (002) plane (Fig. 4d). Overall, it could be concluded that part of the MOF crystals transformed into NiOOH and FeOOH during the OER process, which was similar to the previously reported MOF-based OER catalysts.[22]

In summary, a two-step solvothermal process was rationally designed for the *in situ* fabrication of Ir-NiFe-btz on a NF substrate. The ionic framework of Ir-NiFe-btz improved the overall conductivity of the MOF electrode, the incorporated Ir nanoparticles reduced the OER kinetic barrier by modifying the electronic structure of pristine NiFe-btz, and the synergistic effect between Ni and Fe species contributed to the enhanced OER performances. As a result, Ir-NiFe-btz showed exceptional alkaline OER activity, reaching 10 mA cm^{-2} current density at a low overpotential of 182 mV with a small Tafel slope of 38 mV dec^{-1}. Its remarkable stability was demonstrated by the subtle increase in overpotential throughout the 100 hour stability test. After the OER test, Ir-NiFe-btz was thoroughly characterized and the XPS, SEM and TEM results verified the altered valence states, reconstructed surface structure, and metal oxyhydroxide generation. This work provided a novel approach for designing and fabricating 3D MOF electrodes using the ionic framework with the highly dispersed ultralow level of Ir, broadening the horizons of applying MOFs as OER catalysts.

The authors sincerely thank the Shenzhen Science and Technology Program (KQTD20170810141424366) and Shenzhen Key Laboratory of Advanced Materials Project Engineering (ZDSYS20190911164401990) for supporting this research. H. Z. thanks the University Development Fund (UDF01001057) for supporting his research at CUHK-Shenzhen.

Data availability

The data supporting this article have been included as part of the ESI.†

Conflicts of interest

There are no conflicts to declare.

Notes and references

1 Y. Liu, C. Li, C. Tan, Z. Pei, T. Yang, S. Zhang, Q. Huang, Y. Wang, Z. Zhou and X. Liao, *Nat. Commun.*, 2023, **14**, 2475.
2 W. Li, H. Zhang, K. Zhang, Z. Cheng, H. Chen, G. Tan, X. Feng, L. Wang and S. Mu, *Chem. Commun.*, 2023, **59**, 4750–4753.
3 K. Adpakpang, L. Pukdeejorhor, L. Ngamwongwan, S. Suthirakun, S. Impeng, S. Wannapaiboon, P. Chakthranont, K. Faungnawakij and S. Bureekaew, *Chem. Commun.*, 2022, **58**, 7124–7127.
4 Z. Zhu, W. Hu, X. Wu, Q. Zhang, Y. Hu, Q. Yan, X. Wang and W. Yuan, *J. Colloid Interface Sci.*, 2023, **639**, 274–283.
5 M. Zhao, H. Li, W. Yuan and C. M. Li, *ACS Appl. Energy Mater.*, 2020, **3**, 3966–3977.
6 Y. Jiang, T. Y. Chen, J. L. Chen, Y. Liu, X. Yuan, J. Yan, Q. Sun, Z. Xu, D. Zhang and X. Wang, *Adv. Mater.*, 2024, **36**, 2306910.
7 T. N. Amirabad, A. A. Ensafi, K. Z. Mousaabadi, B. Rezaei and M. Demir, *Int. J. Hydrogen Energy*, 2023, **48**, 29471–29484.
8 N. K. Shrestha, S. A. Patil, A. S. Salunke, A. I. Inamdar and H. Im, *J. Mater. Chem. A*, 2023, **11**, 14870–14877.
9 H. Furukawa, N. Ko, Y. B. Go, N. Aratani, S. B. Choi, E. Choi, A. O. Yazaydin, R. Q. Snurr, M. O'Keeffe and J. Kim, *Science*, 2010, **329**, 424–428.
10 P. Maurya, T. Ansari and A. Indra, *Chem. Commun.*, 2023, **59**, 13359–13362.
11 M. Ding, X. Cai and H.-L. Jiang, *Chem. Sci.*, 2019, **10**, 10209–10230.
12 Q. Wang and D. Astruc, *Chem. Rev.*, 2019, **120**, 1438–1511.
13 Y. Jia, Z. Xu, L. Li and S. Lin, *Dalton Trans.*, 2022, **51**, 5053–5060.
14 L. Zhao, J. Yan, H. Huang, X. Du, H. Chen, X. He, W. Li, W. Fang, D. Wang and X. Zeng, *Adv. Funct. Mater.*, 2024, **34**, 2310902.
15 W.-H. Li, J. Lv, Q. Li, J. Xie, N. Ogiwara, Y. Huang, H. Jiang, H. Kitagawa, G. Xu and Y. Wang, *J. Mater. Chem. A*, 2019, **7**, 10431–10438.
16 C. Cao, D. D. Ma, Q. Xu, X. T. Wu and Q. L. Zhu, *Adv. Funct. Mater.*, 2019, **29**, 1807418.
17 S. Dutta, Y. D. More, S. Fajal, W. Mandal, G. K. Dam and S. K. Ghosh, *Chem. Commun.*, 2022, **58**, 13676–13698.
18 X. Zhao, X. Bu, T. Wu, S.-T. Zheng, L. Wang and P. Feng, *Nat. Commun.*, 2013, **4**, 2344.
19 S. Zhou, Y. Liu, J. Shi, J. Li and W. Cai, *Chem. Commun.*, 2023, **59**, 14459–14462.
20 S. Li, T. Wang, D. Tang, Y. Yang, Y. Tian, F. Cui, J. Sun, X. Jing, D. S. Sholl and G. Zhu, *Adv. Sci.*, 2022, **9**, 2203712.
21 X. Wang, X. Chen, L. Gao, H. Zheng, M. Ji, C. Tang, T. Shen and Z. Zhang, *J. Mater. Chem.*, 2004, **14**, 905–907.
22 S. Li, Z. Wang, T. Wang, Y. Yang, Y. Xiao, Y. Tian, H. Zhu, X. Jing and G. Zhu, *Chem. – Eur. J.*, 2023, **29**, e202301129.